Fabrication of Spinel One-Dimensional Architectures by Single-Spinneret Electrospinning for Energy Storage Applications

Shengjie Peng,[†] Linlin Li,[‡] Yuxiang Hu,[§] Madhavi Srinivasan,[‡] Fangyi Cheng,[§] Jun Chen,[*,§] and Seeram Ramakrishna[*,†]

[†]Department of Mechanical Engineering, National University of Singapore, 117574 Singapore, [‡]School of Materials Science and Engineering, Nanyang Technological University, 639798 Singapore, and [§]Key Laboratory of Advanced Energy Materials Chemistry (Ministry of Education), College of Chemistry, Nankai University, Tianjin 300071, China

ABSTRACT A facile and general method is developed to fabricate one-dimensional (1D) spinel composite oxides with complex architectures by using a facile single-spinneret electrospinning technique. It is found that precursor polymers and heating rates could control the structures of the products, such as 1D solid, nanotube and tube-in-tubes structures. Especially, the tube-in-tube structures have been successfully fabricated for various mixed metal oxide, including $CoMn_2O_4$, $NiCo_2O_4$, $CoFe_2O_4$, $NiMn_2O_4$ and $ZnMn_2O_4$. Benefiting from the unique structure features, the tube-in-tube hollow nanostructures possess superior electrochemical performances in asymmetric supercapacitors and $Li-O_2$ batteries.

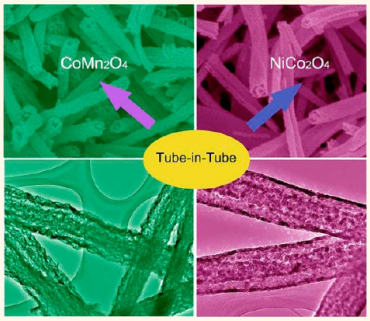

KEYWORDS: electrospinning · hollow structures · spinel · supercapacitors · $Li-O_2$ batteries

The rapid development and ever-growing demand in industry has focused on various applications of functional nanomaterials. The main interest lies in rational control and precise design nanomaterials with specialized morphologies and tailored properties.[1−3] Among various structures, one-dimensional (1D) nanostructure represents one of the most attractive architectures, mainly owing to their intriguing feature and great potential in various applications including catalysis, energy conversion and storage devices, gas sensors, and many others.[4−7] Until now, great success has been achieved in developing effective method to synthesize 1D nanostructures, such as nanofibers, nanobelts, and nanotubes.[8,9] Particularly, tubular nanostructures can be taken as a special 1D structure because of possessing the superiorities of both hollow and 1D structure. This fantasy feature endows them with more competitive power in widespread applications.[10−12] However, most of the tubular 1D structures reported are relatively simple. Consequently, substantial efforts have been devoted to facile synthesis of complex tubular 1D structure, as these complex structures are expected to offer more opportunities to tailor the physical-chemical properties for fundamental studies and practical applications.[13−16] As a case in point, multishelled tubular 1D structure have shown largely improved catalysis and lithium storage properties compared with simple tubular structures.[16] Despite these advances, the synthesis of complex tubular structure is mostly based on templating methods, which is a general method for the fabrication of functional materials with various nanostructures.[17−19] By simple filling (sequential) of porous templates, many kinds of materials can be prepared into 1D hollow structures for various applications. However, the template-directed synthesis is usually tedious and costly, and the quantity of the structures that can be produced in each run of the synthesis is relatively limited. Therefore, the development of straightforward, but general approach for

* Address correspondence to chenabc@nankai.edu.cn, seeram@nus.edu.sg.

Received for review December 2, 2014 and accepted January 20, 2015.

Published online January 20, 2015
10.1021/nn506851x

© 2015 American Chemical Society

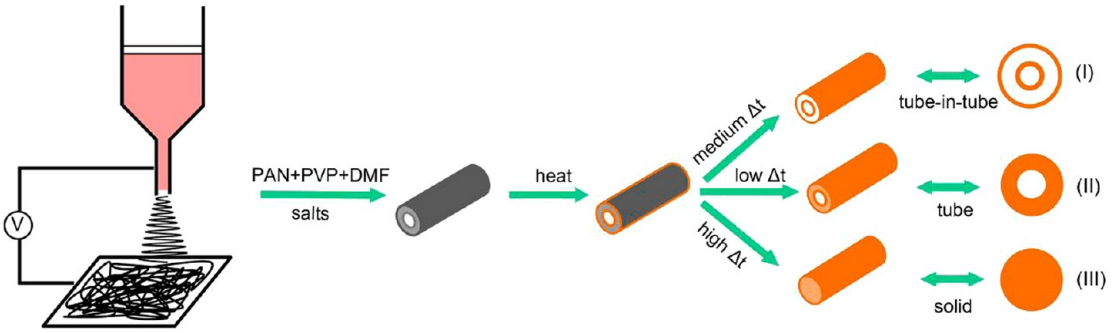

Scheme 1. Schematic illustration for the formation process of the ternary TMOs with complex 1D nanostructures including tube-in-tube, nanotube, and solid 1D nanostructures.

controllable preparation of various functional nanomaterials with complex tubular 1D structure would be highly desirable.

To satisfy the ever-growing energy demand, searching for novel electrode materials for high-performance energy storage devices is always one urgent task. Spinel transition metal oxides (TMOs), especially ternary and mixed oxides, have been intensively investigated and presented promising electrochemical properties as electrode materials for energy conversion and storage systems.[20−25] However, due to the lack of well-defined micro/nanostructures, the electrochemical performance for this kind of TMOs has been largely unsatisfactory. With this in mind, the use of complex tubular 1D nanostructured TMOs is expected to address the above-mentioned issue. On the one hand, complex tubular 1D structure of TMOs could efficiently enhance their performance. On the other hand, complex tubular 1D nanostructures could also found promising applications in many fields, especially energy conversion and storage devices.[26,27] Currently, the preparation of TMOs with complex tubular 1D nanostructure on a large scale by a simple and general approach is unrealized. Hence, the exploration of facile and general strategy for the fabrication of desired TMOs with complex tubular 1D nanostructure still remains great challenge.

As a remarkably simple and versatile technique, electrospinning is believed to be one of the most effective ways to generate 1D nanostructures with different morphologies on a large scale.[28−32] Significantly, although various TMOs nanofibers have been prepared by electrospinning, TMOs with nanotubes or tube-in-tubes architectures are rarely reported. Stimulated by this, herein, we demonstrate a simple and general approach to prepare many various desired ternary TMOs, including $CoMn_2O_4$, $NiCo_2O_4$, $CoFe_2O_4$, $NiMn_2O_4$ and $ZnMn_2O_4$, with complex tubular 1D nanostructures based on an effective single-nozzle electrospinning technique combined with thermal treatment. Remarkably, it is found that the precursor polymers play a key role in forming the hollow structures. More importantly, by rationally adjusting the heating rates, the structure of the as-prepared products can be tuned from 1D solid, nanotubes to tube-in-tube structures. Encouraged by the unique structure features, the application of these tube-in-tube hollow nanostructures in energy storage devices, such as asymmetric supercapacitors and Li−O_2 batteries, demonstrate exceptional electrochemical performances.

RESULTS AND DICUSSION

As schematically illustrated in Scheme 1, the general formation procedure of complex tubular 1D nanostructures ranging from solid 1D structures, hollow, to tube-in-tube structures mainly involves two steps, electrospinning and thermal treatment process. Briefly, the key of these processes is the involvement of two types of polymers during electrospinning and accurate control of the heating rate during thermal treatment. Specifically, in the electrospinning stage, by using different polymer composition, the core−shell precursor fibers, which are suitable to produce tube-in-tube, hollow, and solid 1D nanostructures, can be easily obtained. Initially, a certain amount of different metal precursors (denoted as M), polyvinylpyrrolidone (PVP), and polyacrylonitrile (PAN) are first dissolved in *N*,*N*-dimethylformamide (DMF) solution. Because of the strong coordination ability of PVP to metal ions and the incompatibility of PVP and PAN in DMF solution which is mainly due to the intrinsic properties (*e.g.*, viscosity and interfacial tension),[33,34] the PAN/PVP/M solution undergoes phase separation, leading to the formation of highly stretched PAN core surrounded by PVP/M shell configuration during electrospinning process, as shown in Scheme 1. Besides, the phase separation phenomenon is well supported by Figure S1 (Supporting Information) and also has been demonstrated in previous literature.[35,36] Next, tube-in-tube, nanotube, and solid 1D nanostructure can be obtained after rational controlling nonequilibrium thermal treatment procedure.[37] At a relatively low heating rate, the core−shell electrospun fibers might play a structural directing template role for ensuring the formation of hollow structures. Hereby, the PAN cores would be gradually

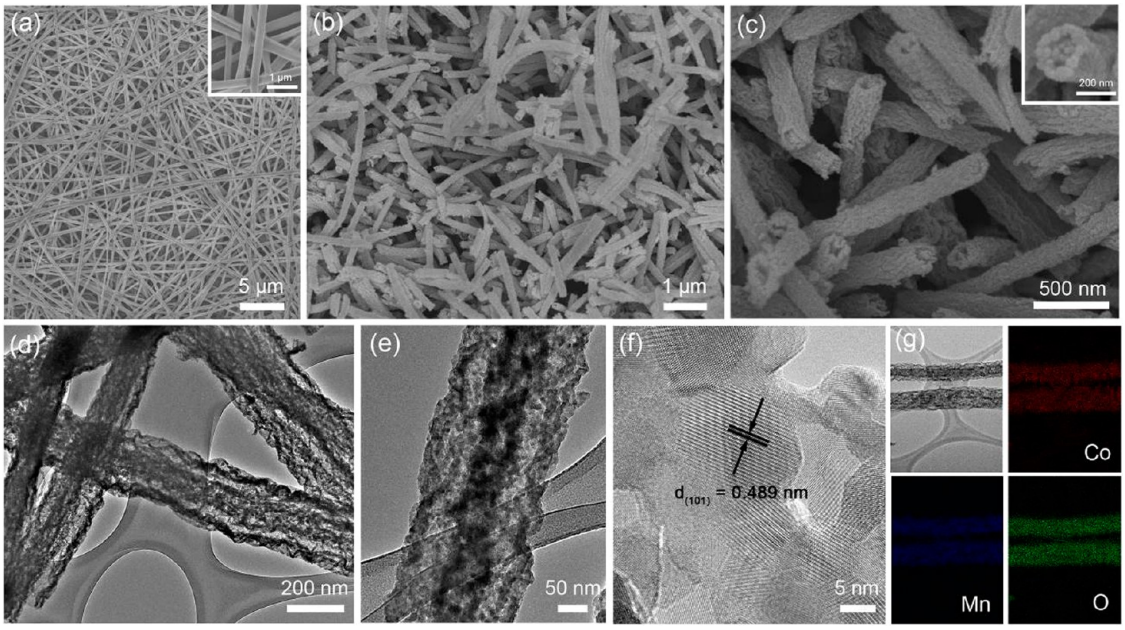

Figure 1. FESEM (a) images of Co−Mn precursor nanofibers; FESEM (b and c), TEM (d and e) and HRTEM (f) images of $CoMn_2O_4$; elemental mapping (g) showing the uniformly distributed Co, Mn, and O element in $CoMn_2O_4$ tube-in-tube nanostructures. The inset shows the corresponding enlarged views.

eliminated, meanwhile the PVP/M shells are homogeneously heated from the surface to the center and shrink into a rigid shell structure together with mass loss of organic component, hence resulting in the hollow tubular structures (as shown in Scheme 1 II). However, with an increasing heating rate, a rigid layer would first form on the outside of PVP/M shell due to the existence of a large temperature gradient (Δt). In the subsequent calcinations, owing to the loss of organic components, the inner gel-like viscoelastic core would continue to undergo intensive shrinkage. Reasonably, the rigid layer would be believed to act as a framework to against the contraction of the outer layer. Spontaneously, it can be imaged that two forces from opposite directions simultaneously act on PVP/M shell. One is the contraction force (F_c), which is induced by the decomposition of organic species and promotes the shrinkage of the PVP/M shell. The other is the adhesive force (F_a) derived from the rigid surface which inhibits its inward contraction.[22,23] By applying a sufficiently high temperature and an appropriate heating rate, namely $F_a \geq F_c$, PVP/M shell could be split into two layers because of the interaction between contraction force and adhesion force, as well as the influence of the kinetic diffusion of metal cations. After complete removal of all the organic components, tube-in-tube structures of phase-pure TMOs can be generated, as shown in Scheme 1 (I). In addition, if the heating rate is so fast, the rigid shells do not have so much time to form. Although the hollow structure might be generated with the decomposition of PAN, the outer layer of precursor electrospun fibers are too viscous at this time and could not retain their hollow structures; thus, the hollow structure would collapse into solid 1D nanostructure, with relatively large diameter compared to the above-mentioned nanotubes and tube-in-tube sturcutres, as shown in Scheme 1 (III). Additionally, Ostwald ripening, which leads to the *in situ* formation of the rigid layer, as well as the kinetics of diffusion of the metal cations, might also be responsible for the generation of tube-in-tube structures. All of these influential factors play an indispensable and important role for the formation of unique hollow tubular structures. In this work, our strategy can be extended to synthesize a relatively wide range of spinel complex 1D tubular nanostructures, which further demonstrate the generality and feasibility of this method.

Five different types TMOs with complex 1D nanostructures, such as $CoMn_2O_4$, $NiCo_2O_4$, $CoFe_2O_4$, $NiMn_2O_4$, and $ZnMn_2O_4$, have been successfully prepared in this work. $CoMn_2O_4$ was taken as an example to demonstrate the unique synthesis procedure. The typical field emission scanning electron microscope (FESEM) images of Co−Mn as-spun precursor nanofibers in Figure 1a and its inset display a smooth surface and continuous uniform features with an average diameter of around 300 nm. After calcination at 600 °C for 2 h, $CoMn_2O_4$ 1D nanostructure can be easily generated. Figure 1b−g shows the FESEM and transmission electron microscope (TEM) images of tube-in-tube structures of $CoMn_2O_4$ obtained at a heating rate of 3 °C min^{-1}, respectively. As observed, the 1D nanostructure can be perfectly maintained and the interesting tube-in-tube structure can be clearly identified from Figure 1b. Obviously, the surface of $CoMn_2O_4$ tube-in-tube structures is quite rough and the

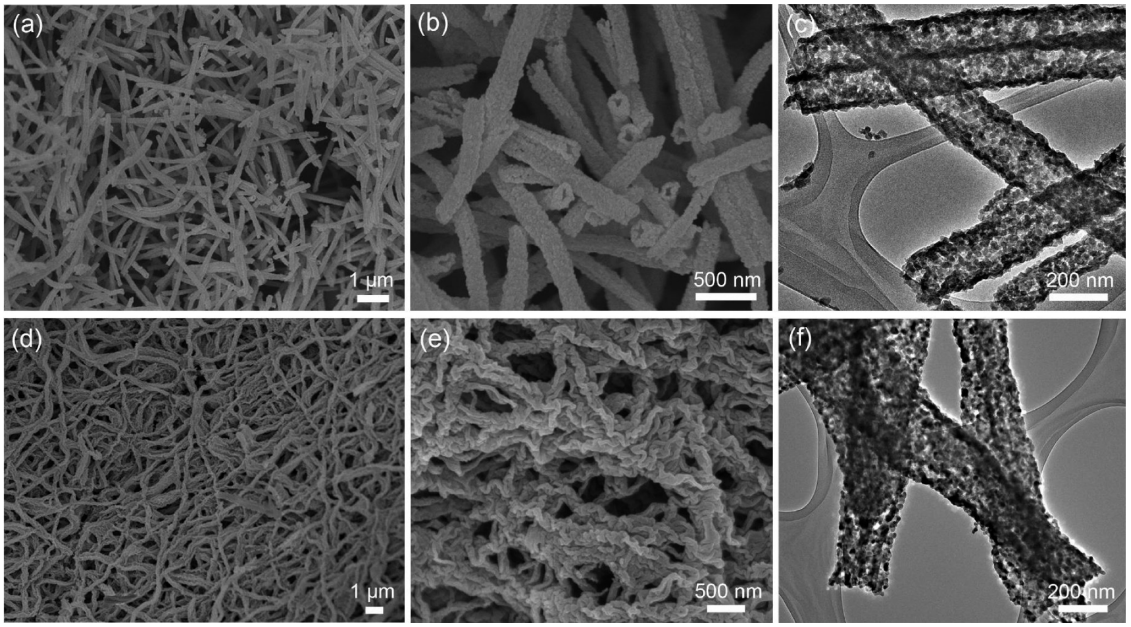

Figure 2. FESEM (a, b, d, and e) and TEM (c and f) images of $CoMn_2O_4$ with the nanotube structure (a−c) and solid 1D nanostructure (d−f), respectively.

diameter decreases to around 227 nm, which might be caused by the decomposition of metal precursor and removal of polymer composition (Figure 1c). Besides, the inset of Figure 1c shows that many nanoparticles constitute the unique tubular structure. The TEM images in Figure 1d and e further confirm the dual tubular structure of $CoMn_2O_4$. It can be clearly seen that the tubular structures possess well-separated walls along nearly their entire length. The average diameter of the outer tubes and inner tube is around 227 and 96 nm, respectively (Figure 1e). The high-resolution TEM (HRTEM) image of $CoMn_2O_4$ tube-in-tube structures in Figure 1f shows a distinct lattice fringes with an interplanar spacing of 0.489 nm, matching well with the (101) planes of $CoMn_2O_4$. The elemental mapping analysis of a single tube-in-tube structure in Figure 1g further certifies the successful preparation of hollow double-wall of the product, and meanwhile proves the coexistence and homogeneous dispersion of Co, Mn, and O elements in the tube-in-tube structures.

More significantly, decreasing the heating rate to 1 °C min^{-1} yields $CoMn_2O_4$ hollow structure with only single wall (Figure 2a−c). Compared to $CoMn_2O_4$ tube-in-tube structures, the diameter of these $CoMn_2O_4$ nanotube reduce to around 188 nm. Nevertheless, further increasing the heating rate to 5 °C min^{-1} leads to the collapse of hollow structure and result in the solid 1D nanostructure with average diameter of around 252 nm, which looks quite like colon (Figure 2d−f). In addition, Powder X-ray diffraction (XRD) (Figure S2, Supporting Information) confirmed that all of the above as-prepared samples can be readily assigned to crystalline $CoMn_2O_4$ (JCPDS card no. 77−0471) without any other detectable phase, indicating the phase purity of the as-prepared samples. As described above, the $CoMn_2O_4$ complex 1D nanostructures can be easily fabricated in large scale with high purity.

Impressively, many other ternary TMOs with complex 1D nanostructures have been successfully synthesized using the described electrospinning technique combined with accurate thermal treatment. All of these provide powerful evidence for the generality of the present synthesis method. Figure 3 displays typical SEM and TEM images of $NiCo_2O_4$ (Figure 3a and b), $CoFe_2O_4$ (Figure 3c and d), $NiMn_2O_4$ (Figure 3e and f), and $ZnMn_2O_4$ (Figure 3g and h) tube-in-tube structures. As can be seen, these four different ternary metal oxides can be obtained in large scale and all of these present almost identical tube-in-tube structures. Similarly, as an example, the elemental mapping analysis of $NiCo_2O_4$ tube-in-tube structures also confirm the unique double-wall structure with uniformly distributed Ni, Co, and O elements and HRTEM image indicates the highly crystalline nature of the $NiCo_2O_4$ nanoparticles (Figure S3, Supporting Information). However, it is worth pointing out that the surface roughness of different materials exhibit slight difference. Apparently, a large amount of pores can be discerned on the surface of $NiCo_2O_4$ and $NiMn_2O_4$, whereas $CoFe_2O_4$ and $ZnMn_2O_4$ appear to be relatively rough surface with dense feature, respectively. It is believed that the distinct crystal growth habits and crystallization behavior of different materials during calcination process might give rise to the diversity in surface.[16] Aside from the tube-in-tube structures, the aforementioned four different materials with nanotube or solid 1D structure can be readily prepared using the same electrospinning procedure as that for $CoMn_2O_4$

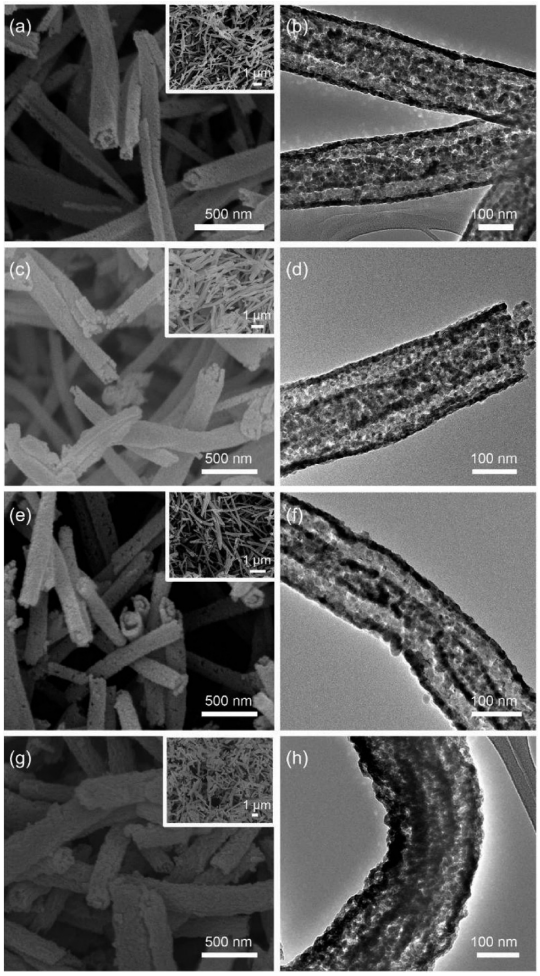

Figure 3. FESEM and TEM images of (a and b) $NiCo_2O_4$, (c and d) $CoFe_2O_4$, (e and f) $NiMn_2O_4$, and (g and h) $ZnMn_2O_4$ with tube-in-tube nanostructure (The inset shows the corresponding large-area view).

complex 1D nanostructures (Figure S4 and Figure S5, Supporting Information). As anticipated, taken $NiCo_2O_4$ nanotubes as an example, the elemental mapping results further attest uniformly distributed Ni, Co, and O elements in $NiCo_2O_4$ nanotubes (Figure S6, Supporting Information). Meanwhile, all the as-prepared samples are correspondingly pure spinel TMOs (Figure S7, Supporting Information). Additionally, the evolution of the complex 1D tubular structure from nanotube, tube-in-tube to 1D solid architectures have also been investigated by employing different heating rates (Figure S8, Supporting Information). These results corroborate our proposed formation mechanism in Scheme 1. All these results confirm the feasibility of our strategy for the construction of complex 1D nanostructure for many different TMOs, which is highly desirable to find broad application in many fields.

In view of that mixed metal oxides have always been regarded as promising functional materials for various applications. Meanwhile, the tube-in-tube structures are expected to dramatically benefit energy-related applications, such as lithium ion batteries (LIBs), supercapacitors (SCs), and lithium-air batteries. Herein, $NiCo_2O_4$ tube-in-tube structures were used as example to demonstrate the superiority of these tube-in-tube structures as electrode for SCs applications. Next, we first performed the electrochemical characterization in a three-electrode configuration using 2.0 M KOH electrolyte. Figure 4a shows the typical cyclic voltammetry (CV) curves of $NiCo_2O_4$ tube-in-tube structures at different scan rate ranging from 1−20 mV s^{-1}. Clearly, the shape of the CV curves confirms the psedocapacitive behavior. Two pairs of poorly defined redox peaks are observed within the potential range of 0−0.4 V (*vs* SCE), which originates from Faradaic redox reactions related to M−O/M−O−OH, where M refers to Ni or Co.[38] Basically, with the increasing scan rate, the peak position shifts slightly, implying the good electrochemical reversibility and excellent high-rate performance. Figure 4b reveals the nonlinear charge/discharge profiles of $NiCo_2O_4$ tube-in-tube structures. The voltage plateaus are in good agreement with the peaks observed in the CV curves. In addition, the specific capacitance derived from the discharge curves is calculated using the formula, $C = I\Delta t/m\Delta V$, where I is the discharge current, Δt represents the discharge time, ΔV is the voltage range and m refers to the mass of active materials. Specifically, the specific capacitance as high as 1756 1697, 1610, 1511, and 1457 F g^{-1} can be obtained at current density of 1, 2, 5, 10, and 20 A g^{-1}, respectively. To further illustrate the superiority of tube-in-tube structures, the electrochemical properties of $NiCo_2O_4$ with nanotube and solid 1D structures were also examined. Similar energy storage mechanisms can be observed from Figure 4c, indicating that the different morphologies make no difference on the faradaic redox reactions. As predicted, $NiCo_2O_4$ tube-in-tube structures demonstrate a better specific capacitance than that of the other samples (Figure 4d). Even at high current density of 20 A g^{-1}, $NiCo_2O_4$ tube-in-tube structures still maintain 83% of the capacitances, suggesting the outstanding rate capability. This is reasonable considering the relatively high specific surface areas of the unique tube-in-tube hollow structures, which is determined to be as high as 47.3 m^2 g^{-1} by Brunauer−Emmett−Teller (BET) analysis compared to 28.0 and 12.9 m^2 g^{-1} for the $NiCo_2O_4$ nanotubes and solid 1D structures, respectively (Figure S9, Supporting Information). In addition, there is a wide pore size distribution for the $NiCo_2O_4$ samples (inset in Figure S9, see the Supporting Information) verifying the porous structure. All of these ensure the electrode/electrolyte contact areas and supply more active sites for fast faradaic redox reactions, thus leading to the superior electrochemical performance. It is well-known that the cycle stability of electrode materials is important parameters for the practical application. As shown in the Figure S10 (see

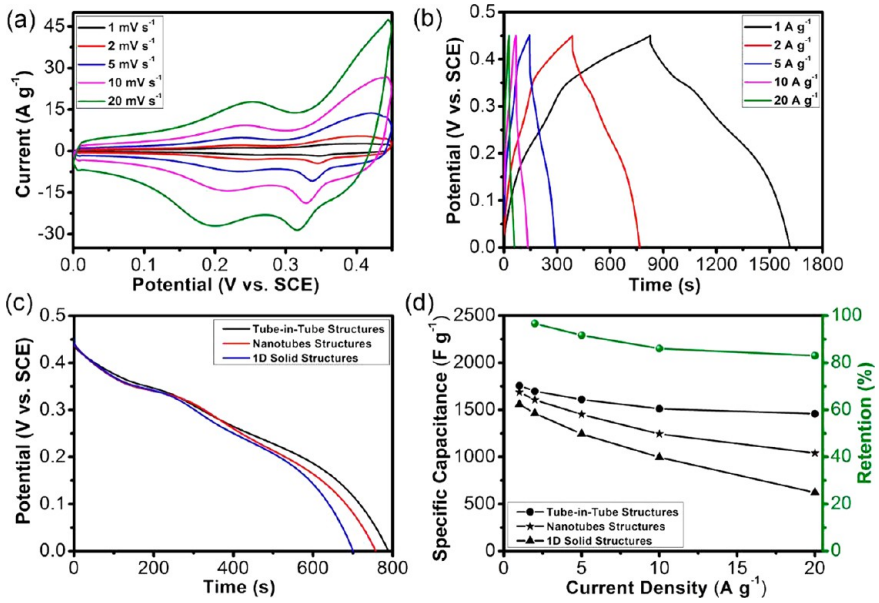

Figure 4. Electrochemical characterizations of $NiCo_2O_4$ nanostructures as electrodes for supercapacitors: CV curves (a) of $NiCo_2O_4$ tube-in-tube nanostructures at various scan rates ranging from 1−20 mV s^{-1}; galvanostatic charge/discharge profiles (b) of $NiCo_2O_4$ tube-in-tube nanostructures at various current densities; discharge profiles (c) of $NiCo_2O_4$ tube-in-tube, nanotube, and 1D solid nanostructures at a current density of 1 A g^{-1}; the specific capacitance (d) at various current density of $NiCo_2O_4$ tube-in-tube, nanotube, and 1D solid nanostructures.

the Supporting Information), it can be found that around 92.4% of the initial specific capacitance still can be delivered even after 5000 cycles at a relatively high current density of 5 A g^{-1}, hence indicating the remarkable long-term electrochemical stability of $NiCo_2O_4$ tube-in-tube structures.

To evaluate the feasibility of such $NiCo_2O_4$ tube-in-tube electrode, an asymmetric supercapacitors (ASCs) device is assembled by using $NiCo_2O_4$ tube-in-tube structure as a positive electrode materials and activated carbon (AC) as the negative electrode. Besides, to achieve the optimized performance of $NiCo_2O_4$ tube-in-tube//AC ASCs device, the optimal mass ratio of positive and negative electrode is fixed to around 0.41, which is based on the charge balance between the two electrodes (Figure S11, Supporting Information). A series of CV measurements in different voltage windows at 20 mV s^{-1} were carried out to estimate the best operating potential of $NiCo_2O_4$ tube-in-tube//AC ASCs device (Figure 5a). With an increase of the operating potential to 1.6 V, no obvious increase of anodic current can be observed, meaning that the electrolyte is stable under such condition. Therefore, 1.6 V is used as the devices potential to further investigate the electrochemical performance of the $NiCo_2O_4$ tube-in-tube//AC ASCs device. Then, CV curves of the ASCs devices at different scan rates ranging from 1−20 mV s^{-1} are given in Figure 5b. A combination of both pseudocapacitive and electric double-layer types of capacitance can be clearly seen at all scan rates. Figure 5c reveals the galvanostatic charge/discharge profiles at different current densities. The discharge curves are almost symmetrical to the corresponding charge curves, suggesting excellent capacitive behavior for the ASCs device. Figure 5d shows the specific capacitance calculated from the discharge curves (based on the total mass both positive and negative electrode). Significantly, the $NiCo_2O_4$ tube-in-tube//AC ASCs device achieves a relatively high specific capacitance of 168 F g^{-1} at the current density of 1 A g^{-1}, which is substantially larger compared to that of recently reported.[39,40] Moreover, the ASCs device exhibits good rate capacitance, with 75% of capacitance retained even at the current density of 20 A g^{-1}.

Figure 5e presents the outstanding cycling stability of the device at current density of 5 A g^{-1} up to 10 000 cycles. It should be noted that the specific capacitance increases gradually during the first 2000 cycles, which is normally related to the presence of the possible activation process. Remarkably, after 10 000 cycles, $NiCo_2O_4$ tube-in-tube//AC ASCs device demonstrates excellent cycling stability and shows around 87% of the specific capacitance retention. Moreover, the charge/discharge curves for the first ten cycles are almost identical, further confirming the outstanding electrochemical reversibility of the device (inset in Figure 5e). Generally, energy density, $E = (C\Delta U^2/2)$ and power density, $P = (E/t)$ are two critical factors for real use of ASCs device. The Ragone plots of $NiCo_2O_4$ tube-in-tube//AC ASCs device derived from the discharge curves are shown in Figure 5f. Impressively, a high energy density of 59.7 Wh kg^{-1} can be obtained at a power density of 800 W kg^{-1} and still retains 44.9 Wh kg^{-1} even at high power density of 16002 W kg^{-1}, which is superior to previously reported systems such as $NiCo_2O_4$// AC,[41] Ni_xCo_{1-x} oxide//AC,[40] and $Ni(OH)_2$-CNT//AC.[42]

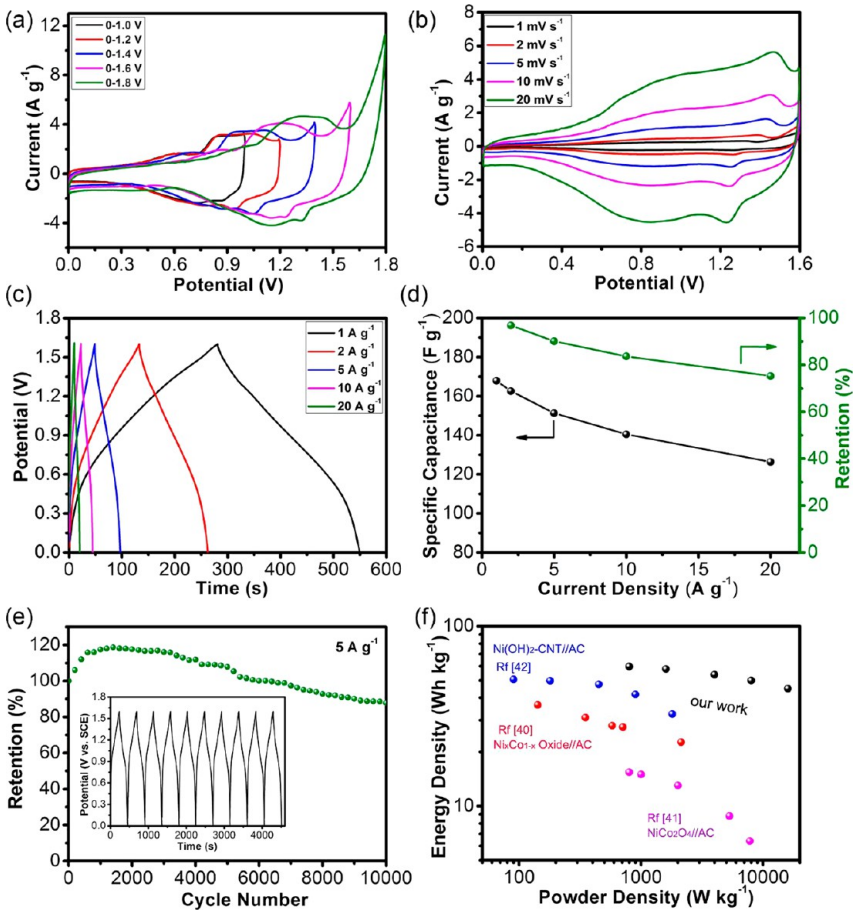

Figure 5. Electrochemical characterizations of $NiCo_2O_4$ tube-in-tube//AC ASCs device: (a) CV curves (a) in various potential window; CV curves (b) at different scan rates; galvanostatic charge/discharge profiles (c) at various current densities; the specific capacitance (d) at various current density and the corresponding capacitance retention; cycling stability (e) of $NiCo_2O_4$ tube-in-tube//AC ASCs device (The inset shows the charge/discharge curves of the first 10 cycles for the ASCs device); Ragone plot (f) of $NiCo_2O_4$ tube-in-tube//AC ASCs device.

Obviously, the exceptional energy density property of $NiCo_2O_4$ tube-in-tube//AC ASCs device might be related to the advantageous tube-in-tube structure. Apparently, the hollow interior of doubly tube structures not only server as "ion-buffering reservoirs" for OH^-, substantially reducing diffusion path of electrons and ions, but also provide sufficient space to buffer the volume variation arising from the high-rate insertion and extraction of OH^-, thus increasing the cycling stability of the electrode. Moreover, the porous feature provides large amount of electroactive sites for fast faradaic reactions, which result in enhanced specific capacitance. Furthermore, 1D structure ensures the rapid transport of electrons and ions, undoubtedly contributing to excellent rate capability of the devices. Combining the above-mentioned superiority, the electrode design of $NiCo_2O_4$ tube-in-tube offers a promising route for high-performance ASCs device.

Next, the $CoMn_2O_4$ with tube-in-tube structures were explored as a typical cathode catalyst in Li—O_2 cells. The discharge and charge curves of the Li—O_2 batteries with $CoMn_2O_4$ mixed with Super P (SP) electrodes are displayed in Figure 6a. It can be observed that the discharge and especially the charge voltage platforms were significantly decreased with the help of the $CoMn_2O_4$ catalyst under a restricting capacity of 1000 mAh g^{-1}_{carbon}. The discharge plateau of $CoMn_2O_4$/SP is higher than that of bare SP by 50 mV, while the charging plateau is found to be much lower than that of SP by about 550 mV. The discharge and charge platforms are among the lowest reported values, indicating its high catalytic activity toward both oxygen reduction reaction (ORR) and oxygen evolution reaction (OER) processes.[43,44] The effect of current densities on the discharge capacities of Li—O_2 batteries with $CoMn_2O_4$ and SP were further investigated. As described in Figure 6b, the $CoMn_2O_4$-based Li—O_2 cell exhibited specific capacities of 5355, 3972, 3074, and 2502 mAh g^{-1}_{carbon} at 100, 200, 400, and 600 mA g^{-1}_{carbon}, which are much higher than those with bare SP at all current densities. Furthermore, the $CoMn_2O_4$ with the tube-in-tube structure presented higher qspecific capacities than $CoMn_2O_4$ with tube and 1D solid structure at a current density of 200 mA g^{-1}_{carbon} (Figure S12, Supporting Information). The obtained much improved specific capacity and rate capability of

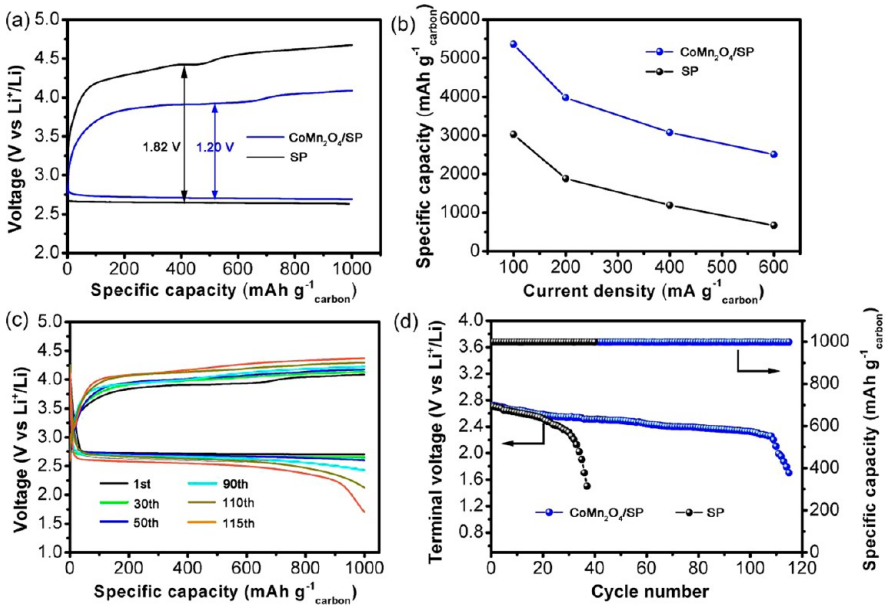

Figure 6. Discharge/charge curves (a) with a restricting capacity of 1000 mAhg$^{-1}_{carbon}$ at a current density of 200 mA g$^{-1}_{carbon}$; discharge specific capacity (b) of Li−O_2 cells with the $CoMn_2O_4$/SP and SP electrodes at different current densities; cycling response (c) and voltage of the terminal discharge *vs* cycle number (d) of the Li−O_2 cell with the $CoMn_2O_4$/SP electrode under specific capacity limit of 1000 mAh g$^{-1}_{carbon}$at a current density of 200 mA g$^{-1}_{carbon}$.

Li−O_2 cells could be attributed to synergistic effect of the high ORR and OER catalytic activity and the unique porous tube-in-tube hollow structure of the $CoMn_2O_4$.

The cycling performance of the $CoMn_2O_4$ cathode was tested at a current density of 200 mA g$^{-1}_{carbon}$ under specific capacity limit of 1000 mAh g$^{-1}_{carbon}$. The $CoMn_2O_4$ electrode could be discharged and charged stably for at least 110 cycles, as shown in Figure 6c and d. No significant changes in the discharge−charge profiles were observed during cycling. On the other hand, the Li−O_2 cell with bare SP electrode can only keep the discharging voltage less than 30th cycle. The improved cycling performance of $CoMn_2O_4$ cathode can be ascribed to the unique tube-in-tube structures of $CoMn_2O_4$ with a relatively high surface area (Figure S13, Supporting Information). The $CoMn_2O_4$ tube-in-tube structures can makes the configured electrode highly porous. Such high porosity can not only provide many electrocatalytic sites and pore volume for nucleation or accommodation of Li_2O_2 discharge products, but also promote the flow of gases and infiltration of the electrolyte, and eventually, improve the capacity and cyclability greatly.[45−47] Furthermore, the cathodes after the first discharge and subsequent charge were analyzed to get valuable information on reaction products formed in Li−O_2 batteries. The X-ray photoelectron spectroscopy (XPS) spectra demonstrate that Li_2O_2 is the main discharge product (Figure S14, Supporting Information). Upon the first discharging, insoluble species precipitate on the surface of the cathode, which are considered as aggregates comprised of nanocrystalline Li_2O_2. After the first charging, the porous structure is essentially regained for the $CoMn_2O_4$/SP electrode (Figure S15, Supporting Information). These results again indicate the superior activity of $CoMn_2O_4$ in catalyzing the oxidation of Li_2O_2 during the recharging process and contribute to enhanced cyclability of the assembled Li−O_2 batteries.

CONCLUSIONS

In summary, we have developed a facile and controllable single-spinneret electrospinning technique to synthesize 1D spinel composite oxides with complex architectures, including $CoMn_2O_4$, $NiCo_2O_4$, $CoFe_2O_4$, $NiMn_2O_4$ and $ZnMn_2O_4$. In this method, the 1D solid, tube and tube-in-tube structures could be easily obtained only by adjusting the precursor polymers and heating rates. This method is quite universal which holds the potential to be further extended to other materials. Encouragingly, we have demonstrated their promising application of the tube-in-tube structure of spinel mixed oxides as electrochemical active materials for asymmetrical supercapacitors and catalysts for Li−O_2 batteries.

EXPERIMENTAL SECTION

Synthesis of Complex 1D Nanostructures. The preparation of ternary TMOs with complex 1D nanostructures involves two steps. Take the preparation of $CoMn_2O_4$ tube-in-tube structures as an example. Briefly, a mixture of 0.5 g of polyvinylpyrrolidone (PVP) and 0.5 g of polyacrylonitrile (PAN) was dissolved in 10 mL of *N*,*N*-dimethylformamide (DMF) solution with stirring to

obtain a homogeneous solution followed by addition of 1 mmol of $Co(CH_3COO)_2$ and 2 mmol of $Mn(CH_3COO)_2$. Subsequently, the mixture was vigorous stirred at room temperature for 24 h, and then a viscous solution can be obtained. Next, the precursor solution was loaded into a plastic syringe with a stainless steel nozzle, which was connected to a high-voltage power supply. A high voltage of 18 kV was applied between the needle tip and aluminum foil collector with a distance of 16 cm and the spinning rate was controlled at 1 mL h^{-1}. Finally, to obtain crystallized $CoMn_2O_4$ with tube-in-tube nanostructure, the obtained as-spun fibers were calcinated at 600 °C for 2 h with a heating rate of 3 °C min^{-1}. By simply changing the heating rate from 1 °C min^{-1} to 5 °C min^{-1}, the structures of $CoMn_2O_4$ can be tuned from nanotube to solid 1D structures, respectively. The synthesis of other ternary metal oxide with complex 1D structure, such as tube-in-tube, nanotubes, and solid 1D structures, is similar to the synthesis of $CoMn_2O_4$ complex 1D structure, by using the respective metal precursors.

Materials Characterization. The morphology of products were characterized using field-emission scanning electron microscope (FESEM; JEOL JSM-7600F), transmission electron microscope (TEM; JEOL JEM-2100F). Investigation of the crystal structure was examined by X-ray diffraction (Shimadzu XRD-6000, Cu Kα radiation, λ = 1.5418 Å). The composition of the Product was analyzed using energy-dispersive X-ray spectroscope (EDX) attached to the TEM instrument. The surface area analysis was carried out using an Autosorb 6B instrument. X-ray photoelectron spectroscopy (XPS) was conducted by Kratos Axis Ultra DLD electron spectrometer at an accelerating voltage of 13 kV and a pass energy of 35.75 eV (PHI, PHI5300 system).

Supercapacitive Measurements. The electrodes were prepared by mixing the electroactive materials (complex 1D $NiCo_2O_4$ nanostructures or activated carbon), conductive carbon (Super−P-Li), and polyvinylidene fluoride (PVDF) in a mass ration of 75:15:10 to obtain slurry. Then, the slurry was pasted onto nickel foam and dried at 80 °C for 10 h under vacuum condition. The electrochemical measurement of the individual electrode were carried out using a three-electrode cell in an aqueous KOH electrolyte (2.0 M), where a standard calomel electrode (SCE) served as reference electrode and a platinum foil as counter electrode. The electrochemical tests of the asymmetric supercapacitor were performed on a two-electrode cell based on $NiCo_2O_4$ electrode as positive electrode and activated carbon (AC) as negative electrode in 2 M KOH aqueous electrolyte solution. The mass loading of active materials is around 1.17 mg cm^{-2}. All of the electorchemical measurements were carried out on Solartron 1470E multichannel potentiostat/cell test system. To assemble an asymmetric supercapacitor, the loading mass ratio of positive and negative electrode was estimated to be 0.41 from the specific capacitance calculated from their CV curves.

Li−O_2 Batteries Measurements. The nonaqueous Li−O_2 cells were prepared using 2032-type coin cell, consisting of an air electrode, a metallic lithium anode, a glass filter separator (What-man), and a 1 M LiTFSi in TEGDME (tetraethylene glycol dimethyl ether) electrolyte. The cathodes were prepared by coating a mixture of catalysts, Super P, and poly(vinylidene fluoride) (PVDF) with weight ratio of 30:60:10 using *N*-methyl-2-pyrrolidinone(NMP) as a dispersing agent onto a circular nickel foam current collector. The total amount is around 0.8 mg cm^{-2}. It should be noted that all the electrodes mass is the same and the active catalyst is about 0.24 mg cm^{-2}. The coated electrode was dried for 12 h at 80 °C under a vacuum to remove any residual solvent. The batteries were then assembled in a glovebox filled with pure argon. The positive top cover was machine-drilled to create 13 evenly distributed 1.5 mm-diameter holes to enable oxygen flow. The Li−O_2 cells were tested in a drybox with desiccants added and O_2 or air was continuously fed into the box. Electrochemical tests were conducted by a LAND-CT2001A battery-testing instrument. The specific capacity and current density were based on the amount of carbon used into the catalysts. The cyclic voltammograms (CVs) were carried out within 2.0−4.6 V at room temperature on parstat 263A workstation (AMETEK).

Conflict of Interest: The authors declare no competing financial interest.

Acknowledgment. We are thankful for the financial support from the Singapore National Research Foundation (NRF-CRP10-2012-06), and China NSFC(21231005) and 973 (2011CB935900).

Supporting Information Available: Photos of the DMF solution containing different polymers, XRD patterns of $CoMn_2O_4$, $NiCo_2O_4$, $CoFe_2O_4$, $NiMn_2O_4$ and $ZnMn_2O_4$ complex 1D structures, EDS mapping and HRTEM image of $NiCo_2O_4$ tube-in-tube nanostructures, SEM and TEM images of $NiCo_2O_4$, $CoFe_2O_4$, $NiMn_2O_4$ and $ZnMn_2O_4$ nanotube and solid 1D structures, N_2 adsorption/desorption isothermals and corresponding pore size distributions of $NiCo_2O_4$ and $CoMn_2O_4$ complex 1D structures, cycling stability of $NiCo_2O_4$ tube-in-tube structure as electrodes at a current density of 5 A g^{-1}, Discharge/charge profiles of the Li−O_2 cells based on $CoMn_2O_4$/SP electrodes at a current rate of 200 mA g^{-1}_{carbon}, XPS spectra and SEM image of discharged and charged $CoMn_2O_4$ cathode. This material is available free of charge *via* the Internet at http://pubs.acs.org.

REFERENCES AND NOTES

1. Hu, J.; Chen, M.; Fang, X.; Wu, L. Fabrication and Application of Inorganic Hollow Spheres. *Chem. Soc. Rev.* **2011**, *40*, 5472–5491.
2. Wang, Z.; Zhou, L.; Lou, X. W. Metal Oxide Hollow Nanostructures for Lithium-ion Batteries. *Adv. Mater.* **2012**, *24*, 1903–1911.
3. Lai, X.; Halpert, J. E.; Wang, D. Recent Advances in Micro-/Nano-Structured Hollow Spheres for Energy Applications: From Simple to Complex Systems. *Energy Environ. Sci.* **2012**, *5*, 5604–5618.
4. Wang, X.; Xie, Z.; Huang, H.; Liu, Z.; Chen, D.; Shen, G. Gas Sensors, Thermistor and Photodetector Based on ZnS Nanowires. *J. Mater. Chem.* **2012**, *22*, 6845–6850.
5. Li, L.; Peng, S.; Cheah, Y.; Ko, Y.; Teh, P.; Wee, G.; Wong, C.; Srinivasan, M. Electrospun Hierarchical $CaCo_2O_4$ Nanofibers with Excellent Lithium Storage Properties. *Chem.—Eur. J.* **2013**, *19*, 14823–14830.
6. Yu, Y.; Gu, L.; Zhu, C.; van Aken, P. A.; Maier, J. Tin Nanoparticles Encapsulated in Porous Multichannel Carbon Microtubes: Preparation by Single-Nozzle Electrospinning and Application as Anode Material for High-Performance Li-Based Batteries. *J. Am. Chem. Soc.* **2009**, *131*, 15984–15985.
7. Shin, J.; Ryu, W. H.; Park, K. S.; Kim, I. D. Morphological Evolution of Carbon Nanofibers Encapsulating SnCo Alloys and Its Effect on Growth of the Solid Electrolyte Interphase Layer. *ACS Nano* **2013**, *7*, 7330–7341.
8. Hochbaum, A. I.; Yang, P. D. Semiconductor Nanowires for Energy Conversion. *Chem. Rev.* **2010**, *110*, 527–546.
9. Lang, L.; Wu, D.; Xu, Z. Controllable Fabrication of TiO_2 1D-Nano/Micro Structures: Solid, Hollow, and Tube-in-Tube Fibers by Electrospinning and the Photocatalytic Performance. *Chem.—Eur. J.* **2012**, *18*, 10661–10668.
10. Wang, Y.; Lee, J. Y.; Zeng, H. C. Polycrystalline SnO_2 Nanotubes Prepared *via* Infiltration Casting of Nanocrystallites and Their Electrochemical Application. *Chem. Mater.* **2005**, *17*, 3899–3903.
11. Zhao, T.; Liu, Z.; Nakata, K.; Nishimoto, S.; Murakami, T.; Zhao, Y.; Jiang, L.; Fujishima, A. Multichannel TiO_2 Hollow Fibers with Enhanced Photocatalytic Activity. *J. Mater. Chem.* **2010**, *20*, 5095–5099.
12. Yu, Y.; Gu, L.; Wang, C.; Dhanabalan, A.; van Aken, P. A.; Maier, J. Encapsulation of Sn@carbon Nanoparticles in Bamboo-like Hollow Carbon Nanofibers as an Anode Material in Lithium-Based Batteries. *Angew. Chem., Int. Ed.* **2009**, *48*, 6485–6489.
13. Gu, Y.; Wu, F.; Wang, Y. Confined Volume Change in Sn-Co-C Ternary Tube-in-Tube Composites for High-Capacity and Long-Life Lithium Storage. *Adv. Funct. Mater.* **2013**, *23*, 893–899.

14. Bavykin, D. V.; Passoni, L.; Walsh, F. C. Hierarchical Tube-in-Tube Structures Prepared by Electrophoretic Deposition of Nanostructured Titanates into a TiO_2 Nanotube Array. *Chem. Commun.* **2013**, *49*, 7007–7009.
15. Bao, Z. Q.; Xie, H.; Zhu, Q.; Qian, J.; Ruan, P.; Zhou, X. Microsphere Assembly of TiO_2 with Tube-in-Tube Nanostructures: Anisotropic Etching and Photovoltaic Enhancement. *CrystEngComm* **2013**, *15*, 8972–8978.
16. Zhang, G.; Xia, B. Y.; Xiao, C.; Yu, L.; Wang, X.; Xie, Y.; Lou, X. W. General Formation of Complex Tubular Nanostructures of Metal Oxides for the Oxygen Reduction Reaction and Lithium-Ion Batteries. *Angew. Chem., Int. Ed.* **2013**, *52*, 8643–8647.
17. Wang, Y.; Angelatos, A. S.; Caruso, F. Template Synthesis of Nanostructured Materials *via* Layer-by-Layer Assembly. *Chem. Mater.* **2007**, *20*, 848–858.
18. Li, X.; Cheng, F.; Guo, B.; Chen, J. Template-Synthesized $LiCoO_2$, $LiMn_2O_4$, and $LiNi_{0.8}Co_{0.2}O_2$ Nanotubes as the Cathode Materials of Lithium Ion Batteries. *J. Phys. Chem. B* **2005**, *109*, 14017–14024.
19. Needham, S. A.; Wang, G. X.; Liu, H. K. Synthesis of NiO Nanotubes for Use as Negative Electrodes in Lithium Ion Batteries. *J. Power Sources* **2006**, *159*, 254–257.
20. Xiong, Q. Q.; Tu, J. P.; Shi, S. J.; Liu, X. Y.; Wang, X. L.; Gu, C. D. Ascorbic Acid-Assisted Synthesis of Cobalt Ferrite ($CoFe_2O_4$) Hierarchical Flower-like Microspheres with Enhanced Lithium Storage Properties. *J. Power Sources* **2014**, *256*, 153–159.
21. Li, L.; Peng, S.; Cheah, Y.; Teh, P.; Wang, J.; Wee, G.; Ko, Y.; Wong, C.; Srinivasan, M. Electrospun Porous $NiCo_2O_4$ Nanotubes as Advanced Electrodes for Electrochemical Capacitors. *Chem.—Eur. J.* **2013**, *19*, 5892–5898.
22. Zhang, G.; Yu, L.; Wu, H. B.; Hoster, H. E.; Lou, X. W. Formation of $ZnMn_2O_4$ Ball-in-Ball Hollow Microspheres as a High-Performance Anode for Lithium-Ion Batteries. *Adv. Mater.* **2012**, *24*, 4609–4613.
23. Zhou, L.; Zhao, D.; Lou, X. W. Double-Shelled $CoMn_2O_4$ Hollow Microcubes as High-Capacity Anodes for Lithium-Ion Batteries. *Adv. Mater.* **2012**, *24*, 745–748.
24. Shen, L.; Che, Q.; Li, H.; Zhang, X. Mesoporous $NiCo_2O_4$ Nanowire Arrays Grown on Carbon Textiles as Binder-Free Flexible Electrodes for Energy Storage. *Adv. Funct. Mater.* **2014**, *24*, 2630–2637.
25. Chen, S.; Qiao, S. Z. Hierarchically Porous Nitrogen-Doped Graphene—$NiCo_2O_4$ Hybrid Paper as an Advanced Electrocatalytic Water-Splitting Material. *ACS Nano* **2013**, *7*, 10190–10196.
26. Song, T.; Xia, J.; Lee, J. H.; Lee, D. H.; Kwon, M. S.; Choi, J. M.; Wu, J.; Doo, S. K.; Chang, H.; Park, W. I.; *et al.* Arrays of Sealed Silicon Nanotubes as Anodes for Lithium Ion Batteries. *Nano Lett.* **2010**, *10*, 1710–1716.
27. Liu, L.; Pippel, E. Low-Platinum-Content Quaternary PtCu-CoNi Nanotubes with Markedly Enhanced Oxygen Reduction Activity. *Angew. Chem., Int. Ed.* **2011**, *50*, 2729–2733.
28. Zhu, Y.; Han, X.; Xu, Y.; Liu, Y.; Zheng, S.; Xu, K.; Hu, L.; Wang, C. Electrospun Sb/C Fibers for a Stable and Fast Sodium-Ion Battery Anode. *ACS Nano* **2013**, *7*, 6378–6386.
29. Li, D.; Xia, Y. Fabrication of Titania Nanofibers by Electrospinning. *Nano Lett.* **2003**, *3*, 555–560.
30. Von Hagen, R.; Lorrmann, H.; Möller, K. C.; Mathur, S. Electrospun $LiFe_{1-y}Mn_yPO_4$/C Nanofiber Composites as Self-Supporting Cathodes in Li-Ion Batteries. *Adv. Energy Mater.* **2012**, *2*, 553–559.
31. Shin, J.; Choi, S. J.; Lee, I.; Youn, D. Y.; Park, C. O.; Lee, J. H.; Tuller, H. L.; Kim, I.-D. Thin-Wall Assembled SnO_2 Fibers Functionalized by Catalytic Pt Nanoparticles and their Superior Exhaled-Breath-Sensing Properties for the Diagnosis of Diabetes. *Adv. Funct. Mater.* **2013**, *23*, 2357–2367.
32. Jeong, G.; Kim, J. G.; Park, M. S.; Seo, M.; Hwang, S. M.; Kim, Y. U.; Kim, Y. J.; Kim, J. H.; Dou, S. X. Core—Shell Structured Silicon Nanoparticles@TiO_{2-x}/Carbon Mesoporous Microfiber Composite as a Safe and High-Performance Lithium-Ion Battery Anode. *ACS Nano* **2014**, *8*, 2977–2985.
33. Zhang, Z.; Li, X.; Wang, C.; Fu, S.; Liu, Y.; Shao, C. Polyacrylonitrile and Carbon Nanofibers with Controllable Nanoporous Structures by Electrospinning. *Macromol. Mater. Eng.* **2009**, *294*, 673–678.
34. Tang, K.; Yu, Y.; Mu, X.; van Aken, P. A.; Maier, J. Multichannel Hollow TiO_2 Nanofibers Fabricated by Single-Nozzle Electrospinning and Their Application for Fast Lithium Storage. *Electrochem. Commun.* **2013**, *28*, 54–57.
35. Lee, B. S.; Son, S. B.; Park, K. M.; Lee, G.; Oh, K. H.; Lee, S. H.; Yu, W. R. Effect of Pores in Hollow Carbon Nanofibers on Their Negative Electrode Properties for a Lithium Rechargeable Battery. *ACS Appl. Mater. Interfaces* **2012**, *4*, 6702–6710.
36. Zhang, Z.; Li, X.; Wang, C.; Wei, L.; Liu, Y.; Shao, C. ZnO Hollow Nanofibers: Fabrication from Facile Single Capillary Electrospinning and Applications in Gas Sensors. *J. Phys. Chem. C* **2009**, *113*, 19397–19403.
37. Mou, F.; Guan, J. G.; Shi, W.; Sun, Z.; Wang, S. Oriented Contraction: A Facile Nonequilibrium Heat-Treatment Approach for Fabrication of Maghemite Fiber-in-Tube and Tube-in-Tube Nanostructures. *Langmuir* **2010**, *26*, 15580–15585.
38. Wu, H. B.; Pang, H.; Lou, X. W. Facile Synthesis of Mesoporous $Ni_{0.3}Co_{2.7}O_4$ Hierarchical Structures for High-Performance Supercapacitors. *Energy Environ. Sci.* **2013**, *6*, 3619–3626.
39. Xu, K.; Li, W.; Liu, Q.; Li, B.; Liu, X.; An, L.; Chen, Z.; Zou, R.; Hu, J. Hierarchical Mesoporous $NiCo_2O_4$@MnO_2 Core-Shell Nanowire Arrays on Nickel Foam for Aqueous Asymmetric Supercapacitors. *J. Mater. Chem. A* **2014**, *2*, 4795–4802.
40. Wang, Y. M.; Zhang, X.; Guo, C. Y.; Zhao, Y. Q.; Xu, C. L.; Li, H. L. Controllable Synthesis of 3D Ni_xCo_{1-x} Oxides with Different Morphologies for High-Capacity Supercapacitors. *J. Mater. Chem. A* **2013**, *1*, 13290–13300.
41. Lu, X. F.; Wu, D. J.; Li, R. Z.; Li, Q.; Ye, S. H.; Tong, Y. X.; Li, G. R. Hierarchical $NiCo_2O_4$ Nanosheets@Hollow Microrod Arrays for High-Performance Asymmetric Supercapacitors. *J. Mater. Chem. A* **2014**, *2*, 4706–4713.
42. Tang, Z.; Tang, C. H.; Gong, H. A High Energy Density Asymmetric Supercapacitor from Nano-architectured $Ni(OH)_2$/Carbon Nanotube Electrodes. *Adv. Funct. Mater.* **2012**, *22*, 1272–1278.
43. Han, X.; Hu, Y.; Yang, J.; Cheng, F.; Chen, J. Porous Perovskite $CaMnO_3$ as an Electrocatalyst for Rechargeable Li-O_2 Batteries. *Chem. Commun.* **2014**, *50*, 1497–1499.
44. Ryu, W. H.; Yoon, T. H.; Song, S. H.; Jeon, S.; Park, Y. J.; Kim, I. D. Bifunctional Composite Catalysts Using Co_3O_4 Nanofibers Immobilized on Nonoxidized Graphene Nanoflakes for High-Capacity and Long-Cycle Li—O_2 Batteries. *Nano Lett.* **2013**, *13*, 4190–4197.
45. Wang, H.; Yang, Y.; Liang, Y.; Zheng, G.; Li, Y.; Cui, Y.; Dai, H. Rechargeable Li-O_2 Batteries with a Covalently Coupled $MnCo_2O_4$-Graphene Hybrid as an Oxygen Cathode Catalyst. *Energy Environ. Sci.* **2012**, *5*, 7931–7935.
46. Xu, J. J.; Xu, D.; Wang, Z. L.; Wang, H. G.; Zhang, L. L.; Zhang, X. B. Synthesis of Perovskite-Based Porous $La_{0.75}Sr_{0.25}MnO_3$ Nanotubes as a Highly Efficient Electrocatalyst for Rechargeable Lithium—Oxygen Batteries. *Angew. Chem., Int. Ed.* **2013**, *52*, 3887–3890.
47. Cheng, F. Y.; Chen, J. Metal-air batteries: from oxygen reduction electrochemistry to cathode catalysts. *Chem. Soc. Rev.* **2012**, *41*, 2172–2192.